Journal of Materials Chemistry B

ROYAL SOCIETY OF CHEMISTRY

PAPER

View Article Online
View Journal | View Issue



Check for updates

Cite this: J. Mater. Chem. B, 2024, 12, 3144

# Evaluation of gelatin-based hydrogels for colon and pancreas studies using 3D *in vitro* cell culture†

Regina Pamplona, [a] Sandra González-Lana, [bc] Ignacio Ochoa, [cde] Rafael Martín-Rapún *[adf] and Carlos Sánchez-Somolinos *[dg]

Biomimetic 3D models emerged some decades ago to address 2D cell culture limitations in the field of replicating biological phenomena, structures or functions found in nature. The fabrication of hydrogels for cancer disease research enables the study of cell processes including growth, proliferation and migration and their 3D design is based on the encapsulation of tumoral cells within a tunable matrix. In this work, a platform of gelatin methacrylamide (GelMA)-based photocrosslinked scaffolds with embedded colorectal (HCT-116) or pancreatic (MIA PaCa-2) cancer cells is presented. Prior to cell culture, the mechanical characterization of hydrogels was assessed in terms of stiffness and swelling behavior. Modifications of the UV curing time enabled a fine tuning of the mechanical properties, which at the same time, showed susceptibility to the chemical composition and crosslinking mechanism. All scaffolds displayed excellent cytocompatibility with both tumoral cells while eliciting various cell responses depending on the microenvironment features. Individual and collective cell migration were observed for HCT-116 and MIA PaCa-2 cell lines, highlighting the ability of the colorectal cancer cells to cluster into aggregates of different sizes governed by the surrounding matrix. Additionally, metabolic activity results pointed out to the development of a more proliferative phenotype within stiffer networks. These findings confirm the suitability of the presented platform of GelMA-based hydrogels to conduct 3D cell culture experiments and explore biological processes associated with colorectal and pancreatic cancer.

Received 7th November 2023,
Accepted 1st March 2024

DOI: 10.1039/d3tb02640j

rsc.li/materials-b

## Introduction

Since the first biomimetic strategies in cell culture, the goal of recreating basic aspects of the tumor microenvironment (TME) has been significantly targeted. This surrounding microenvironment comprises different cell types, soluble factors and a complex and dynamic extracellular matrix (ECM). In addition, the composition of the ECM within which cells reside is continuously changing, and some factors, such as increased stiffness, have been related to the development of the cancer disease.[1] In this context, colorectal cancer (CRC) *in vitro* studies, such as the one performed by Tang *et al.*,[2] demonstrated that the alteration of microenvironment stiffness is among the signaling pathways implicated in the initiation of metastasis. Likewise, pancreatic ductal adenocarcinoma (PDAC) is characterized by a particularly pronounced deposition of a dense ECM. Rice and co-workers[3] reported how the increasing stiffness of polyacrylamide gels promoted different elements of the epithelial–mesenchymal transition (EMT) in pancreatic cancer cell lines.

When considering different biomimetic models, two-dimensional (2D) cell culture studies provide a straightforward, low-cost and high-performance approach to explore cancer biology. Unfortunately, cell–cell interactions established in 2D *in vitro* experiments are different from how cells would

[a] Aragón Institute of Nanoscience and Materials (INMA), CSIC-University of Zaragoza, Department of Organic Chemistry, C/Pedro Cerbuna 12, 50009 Zaragoza, Spain. E-mail: rmartin@unizar.es
[b] BEONCHIP S.L., CEMINEM, Campus Río Ebro. C/Mariano Esquillor Gómez s/n, 50018 Zaragoza, Spain
[c] Tissue Microenvironment (TME) Lab. Aragón Institute of Engineering Research (I3A), University of Zaragoza, C/Mariano Esquillor s/n, 500018 Zaragoza, Spain
[d] CIBER in Bioengineering, Biomaterials and Nanomedicine (CIBER-BBN), Madrid, Spain
[e] Institute for Health Research Aragón (IIS Aragón), Paseo de Isabel La Católica 1-3, 50009 Zaragoza, Spain
[f] Universidad de Zaragoza, Facultad de Ciencias, Departamento de Química Orgánica, C/Pedro Cerbuna 12, 50009 Zaragoza, Spain
[g] Aragón Institute of Nanoscience and Materials (INMA), CSIC-University of Zaragoza, Department of Condensed Matter Physics (Faculty of Science), C/Pedro Cerbuna 12, 50009 Zaragoza, Spain. E-mail: carlos.s@csic.es

† Electronic supplementary information (ESI) available. See DOI: https://doi.org/10.1039/d3tb02640j

experience in a three-dimensional (3D) environment. This is partly because 2D substrates lack the ability to mimic geometrical confinement or shear stress.[4,5] In fact, a two-way communication exists between cells and their surrounding microenvironment, and investigating these cell–matrix interactions in a 3D context constitutes a more physiologically relevant approach.

Amidst the broad domain of 3D scaffolds, gelatin methacrylamide (GelMA) hydrogels have gained increasing attention ever since the initial report from Van Den Bulcke *et al.*[6] These hydrogels originate from a natural polymer, incorporate the cell-adhesive arginine–glycine–aspartic acid (RGD) sequence, and offer extensive photocrosslinking possibilities to achieve tailor-made scaffolds.[7] While this material has been particularly useful in breast cancer tumor models,[8,9] there are limited studies applied to colon and pancreas and those works are primarily focused on drug screening.[10,11]

Regarding photo-induced crosslinking reactions which allow for finely-tuned control of biomechanics in hydrogels, the free radical photopolymerization approach stands out as one of the simplest and most rapid method to generate 3D scaffolds.[12,13] Nevertheless, GelMA also has the potential to form hydrogels by combining with other photocrosslinkable functional groups, such as allyl[14] and diacrylates[5] as well as thiol motifs, through a process known as photoclick chemistry.[15–17] These thiol-based reactions are orthogonal, highly selective and efficient, yielding the final molecule without any by-products.[18] However, when it comes to studies focused on colorectal and pancreatic cancer, there are only a few examples in the literature that demonstrate the use of gelatin-containing hydrogels crosslinked *via* thiol–ene reactions.[12,19,20] In our previous work, we reported the effectiveness of the methacrylate-thiol system (GelMA + 4-arm PEG thiol) as a robust platform for easily tuning hydrogel mechanics. Furthermore, we also confirmed excellent cell viability using semi-3D models (colorectal epithelial cells grown on top of 3D substrates).[17]

The biomaterials community has shown considerable interest in using 3D cell culture hydrogels to replicate the TME as a means of obtaining a more comprehensive understanding of cancer progression. During this culture process, cells grow and proliferate within a mechanical landscape which is constantly being remodeled. Reproducing the dynamic state of the ECM is a challenging task. However, a number of works focused on the structural architecture, mechanical and biochemical functions can be found in literature, offering valuable insights into cancer research. Referring to colorectal cancer biomimetic studies, Cadamuro and co-workers prepared hyaluronic acid-based hydrogels through 3D bioprinting and they described how the glycosylation of ECM proteins induced several alterations to the proteome of the encapsulated HT-29 cells.[21] Williams *et al.* reported that HCT-116 cells displayed a different phenotype when embedded into fiber-reinforced agarose hydrogels as a result of morphological guidance.[22] As well, Jabbari and co-workers found that HCT-116 cells underwent phenotypic changes towards a more aggressive and invasive behavior due to an increase in matrix stiffness.[23] Similarly, in the context of pancreatic cancer research, Betriu *et al.* elucidated how the stiffness of self-assembling peptide scaffolds influenced cellular responses. These authors reported that increased matrix stiffness led to downregulation of focal adhesion kinase (FAK) in PDAC cells.[24] In addition, Puls and co-workers encapsulated MIA PaCa-2 cells within collagen hydrogels of varying fibril density and matrix stiffness. They subsequently observed significant changes in cell morphology and proteins expression.[25]

Despite the efforts of the scientific community, a significant demand remains for the development of biomimetic models tailored to the specific needs of PDAC and colorectal cancer research, in order to further advance our understanding of these diseases. In this study, we exploit our developed methacrylate-thiol system (GelMA + 4-arm PEG thiol) platform to fabricate cell-embedded 3D scaffolds for colorectal and pancreatic cancer research. We aim to investigate how the composition and the hydrogel stiffness influence the cell viability, migration and proliferation of HCT-116 and MIA PaCa-2 cells lines. Cell-free GelMA-based hydrogels were first characterized in terms of swelling behavior and stiffness using atomic force spectroscopy (AFM) measurements. Subsequently, after encapsulating cells, the cell-laden hydrogels were assessed at both day 1 and day 3 for cell viability, mitochondrial activity and DNA content. Furthermore, to study cell migration, the cell-laden hydrogels were placed in the IncuCyte® live-imaging system and continuously monitored in real-time over the course of the 3 days of cell culture assay.

## Materials and methods

### Materials

Gelatin from porcine skin (type A, 300 Bloom), methacrylic anhydride (MAA) (94%), 3-(trimethylsilyl)propionic-2,2,3,3-$d_4$ acid sodium salt (TMSP), dialysis tubing cellulose membranes (MWCO: 12–14 kDa), 2,4,6-trinitrobenzenesulfonic acid 5% w/v solution (TNBS), sodium *n*-dodecyl sulfate 20% w/v solution (SDS), glycine (ReagentPlus, ≥99%), photoinitiator 2-hydroxy-4′-(2-hydroxyethoxy)-2-methylpropiophenone, also known as Irgacure 2959 (I2959), NaOH 1 N and DMEM 5× were obtained from Sigma Aldrich. Deuterium oxide was purchased from Eurisotop. 4-Arm poly(ethylene glycol) thiol (4PEGSH) was supplied by JenKem, USA. Poly(dimethylsiloxane) (PDMS) elastomer was prepared from Sylgard-184 (Dow Corning). Type I rat tail collagen (10.9 mg $mL^{-1}$) was purchased from Corning, USA. Phosphate buffered saline (PBS) pH 7.4, high glucose Dulbecco's modified eagle's medium (DMEM) without Phenol red, Advanced DMEM, Glutamax, penicillin/streptomycin (10 000 U $mL^{-1}$) and non-essential amino acids (10×) were purchased from Gibco, Life Technologies. Fetal bovine serum (FBS), trypsin, Calcein AM (CAM), propidium iodide (PI) and Triton X-000 were obtained from Sigma-Aldrich. 3-(4,5-Dimethylthiazol-2-yl)-5-(3-carboxymethoxyphenyl)-2-(4-sulfophenyl)-2*H*-tetrazolium (MTS) reagent was supplied by Abcam. Paraformaldehyde and peqGold Blood & Tissue DNA Mini Kit

protocol were purchased from VWR. Fluorescent dyes Cell Tracker Orange CMTMR, 4′,6-diamidino-2-phenylindole (DAPI) and Alexa Fluor 488 Phalloidin were supplied by Invitrogen. All purchased materials were used without further purification.

### GelMA synthesis

Gelatin methacrylamide was synthesized on a 3-gram scale according to Shirahama *et al.*[26] In brief, a 10% w/v solution of type A gelatin (300 Bloom) in carbonate–bicarbonate (CB) buffer (0.25 M, pH 9) was prepared. The solution contained in a round-bottom flask was heated in an oil bath at 50 °C for 20 min without stirring, and then vigorously stirred for 1 h until complete dissolution. Next, methacrylic anhydride (MAA) was added dropwise to the gelatin solution with an amine : MAA feed molar ratio of 1 : 1.5, where the free amino groups of gelatin were determined following the Habeeb method[27] also used by Van Den Bulcke *et al.*[6] The reaction was allowed to continue under stirring at 50 °C for 3 h. Afterward, the pH was adjusted to 7.4 to halt the methacrylation reaction. The resulting solution was dialyzed against distilled water using dialysis membranes. Dialysis took place inside an incubator at 37 °C with gentle orbital shaking and was performed four times within 24 h to remove salts, methacrylic acid, and anhydride. Following purification, the product was subjected to an overnight freezing at −80 °C. Finally, it was lyophilized for 1 week and stored at −20 °C, shielded from light until further use.

### NMR spectroscopy

NMR spectra were acquired at room temperature (RT) using a Bruker AV-400 spectrometer and operating at a proton Larmor frequency of 400.16 MHz. Both gelatin and GelMA macromer samples were prepared at a final concentration of 25 mg $mL^{-1}$ in deuterium oxide. To serve as an internal standard, TMSP was employed at a concentration of 1 mg $mL^{-1}$. Data processing was conducted using MestReNova software.

### Degree of functionalization: TNBS assay

The degree of functionalization (DF) was determined as the percentage of amino groups (originating from lysine and hydroxylysine) derivatized in GelMA, as described in literature.[28] The quantification involved measuring the remaining free amino groups using TNBS based on Habeeb method[27] and Lee *et al.* modifications.[29] Each sample was prepared in duplicate following the outlined protocol. In brief, separate solutions of GelMA and gelatin were dissolved in 0.1 M CB buffer pH 8.5, with concentrations of 5 mg $mL^{-1}$ for GelMA and 1 mg $mL^{-1}$ for gelatin. Next, 50 μL of each gelatin solution were pipetted into 96-well plates and 25 μL of 0.1% w/v TNBS were added. Microwell plate was then incubated for 2.5 h at 37 °C in the dark with gentle shaking to allow the nucleophilic substitution and formation of the yellow-colored amine derivative.[30] After incubation, 25 μL of 10% w/v SDS solution and 12.5 μL of 1 M HCl were added to each sample to stop the reaction. The absorbance of samples was measured at 330 nm using a microwell plate reader (Multiskan Go, Thermo Scientific). A glycine standard curve was used to calculate the amino group content with standard sample solutions prepared at 0, 0.16, 0.32, 0.48, 0.64, 0.72 mM. All glycine solutions were subjected to the same TNBS procedure as GelMA samples. DF was calculated as shown in the following formula:

$$\mathrm{DF} = \left( \frac{\text{amino content gelatin}\left(\frac{\text{mmol}}{\text{g}}\right) - \text{amino content GelMA}\left(\frac{\text{mmol}}{\text{g}}\right)}{\text{amino content gelatin}\left(\frac{\text{mmol}}{\text{g}}\right)} \right) \times 100$$

### Hydrogels preparation

GelMA hydrogels were formed through free radical photopolymerization of the GelMA macromer in high glucose DMEM supplemented with 1% penicillin/streptomycin and 1% v/v of non-essential amino acids (named as DG0 throughout the manuscript), along with a photoinitiator. During photopolymerization, undesirable effects such as UV light absorption and attenuation may be generated by the presence of phenol red in cell culture media.[31] For this reason, gelatin-based solutions were all prepared in DMEM without phenol red, with a final concentration of 6% w/v GelMA macromer and 0.1% w/v I2959. The hydrogel precursor mixture in DG0 was incubated at 37 °C for 1 h while protected from light to ensure complete dissolution. In the case of GelMA–SH hydrogels, 5% w/v 4-arm PEG thiol solution in DG0 was then added to the mixture at a final functional group ratio methacrylamide : SH 1 : 0.5. As presented in our previous work,[17] PDMS molds with two different dimensions enabled the fabrication of hydrogels for mechanical testing. AFM measurements were performed with disc-shaped scaffolds hydrogels ($D$ = 10 mm, thickness = 1 mm) prepared by pouring 120 μL of mixture into PDMS molds mounted on top of glass slides. On the other hand, 130 μL of GelMA hydrogel precursor were used to fabricate cylindrical hydrogels ($D$ = 6 mm, thickness = 3 mm) for swelling experiments. Subsequently, hydrogels were incubated at RT for 20 min to allow for physical gelation. Finally, hydrogels were exposed to UV light (320–390 nm, 10 mW $cm^{-2}$) for 10 s, 30 s or 150 s using and OmniCure S2000 UV Lamp, resulting in the formation of the final photopolymerized hydrogels. The UV time applied to each hydrogel is indicated in the name given to each material, *i.e.* for GelMA-30 the mixture was exposed to UV light for 30 s.

To create the control collagen hydrogels, a mixture was made by combining 10.9 mg $mL^{-1}$ of type I rat tail collagen with 1 N NaOH and DMEM 5× in a proportion of 1 : 40 and 1 : 8 (v/v of collagen volume), respectively. After pouring the warm mixture into the PDMS molds, collagen hydrogels were physically crosslinked at 37 °C for 20 min inside an incubator. Furthermore, to include the UV condition in the control

 

samples, some collagen hydrogels were irradiated with the maximum UV time employed within this work, that is, 150 s.

All the protocols with collagen, GelMA and GelMA–SH mixtures were performed under sterile conditions.

### Hydrogels characterization

**Swelling behavior.** After hydrogel crosslinking, samples were frozen in liquid nitrogen and lyophilized overnight. Freeze-dried hydrogels were then weighed ($W_{d1}$) and submerged in DG0 at 37 °C for 24 h to dissolve the unbounded polymer gelatin chains from the network. After incubation, the excess of DG0 was blotted by KimWipes. Next, hydrogels were frozen in liquid nitrogen, lyophilized overnight and weighed again to determine the final dry mass ($W_{d2}$). The changes in mass between $W_{d1}$ and $W_{d2}$ define the percentage of material which is chemically crosslinked and incorporated in the ultimate 3D network. Thus, gel fraction (%) was derived using the following formula:

$$\text{Gel fraction } (\%) = \frac{W_{d2}}{W_{d1}} \times 100$$

On the other hand, the hydrogel swelling ratio refers to its capacity to absorb an aqueous medium. The experimental protocol to assess the mass swelling ratio (MSR) began with the incubation of photocrosslinked hydrogels in DG0 at 37 °C for 24 h under sterile conditions. Then, the excess of DG0 was gently removed with a Kimwipe paper and samples were weighed ($W_s$). Finally, the dry mass of hydrogels ($W_d$) was recorded after freezing in liquid nitrogen and lyophilizing overnight. MSR (g g$^{-1}$) was defined as:

$$\text{Mass swelling ratio } \left(\text{g g}^{-1}\right) = \frac{W_s}{W_d}$$

Three replicate samples of each condition were tested for all calculations regarding gel fraction and MSR.

**Mechanical testing: atomic force spectroscopy.** AFM measurements were conducted in contact mode using a NanoWizard 3 AFM module (JPK Instruments AG, Germany), which was paired with an optical inverted microscope (Nikon-Eclipse). For nanoindentation experiments, qp-BioAC-CB1 probes (Nanosensors, Switzerland) with a nominal spring constant of 0.3 N m$^{-1}$ were utilized. Prior to AFM experiments, the cantilever was calibrated as recommended for mechanical testing. The specific spring constant was determined using the thermal noise method. Measurements were performed in DG0 at 37 °C, and a Petri dish heater (JPK Instruments AG, Germany) was employed to maintain the temperature. To prevent disc-shaped hydrogels from floating and interfering with nanoindentation, they were cured directly onto a glass substrate, ensuring their stability. After incubation in DG0 at 37 °C for 24 h, the hydrogels were placed in a Petri dish filled with tempered cell culture media. Scan rate was set at 2 μm s$^{-1}$ and force–distance curves were recorded up to a force setpoint of 1 nN. Force mappings with an 8 × 8 pixel resolution were acquired over a 10 × 10 μm area, and three to four maps were recorded per sample. Young's Moduli of hydrogels were extracted by fitting the approach curves to the Hertz model, approximating the tip as a 15° cone, using the AFM software (JPK SPM Desktop – Nanowizard). For statistical analysis, three samples of each condition were tested to calculate means and standard deviations.

### Cell culture

For 3D *in vitro* cell culture experiments, hydrogels were directly prepared in 96 well-plates. HCT-116 and MIA PaCa-2 cells were cultured in flasks in Advanced DMEM supplemented with 10% v/v FBS and 1% penicillin/streptomycin (named as DG10 throughout the manuscript). Cells were maintained at 37 °C in a humidified incubator with 5% $CO_2$ (standard conditions), exchanging the medium every 2–3 days until they reached 90% confluence. For the fabrication of cell-laden hydrogels, HCT-116 and MIA PaCa-2 cells were first trypsinized, counted and re-suspended in DG10. Following centrifugation, the pellet cells were resuspended in warm mixtures of collagen, GelMA, or GelMA–SH to achieve a final density of 4 × 10$^6$ cells per mL. For GelMA and GelMA–SH hydrogels, each well was filled with 50 μL of the cell mixture, and the well plates were incubated at RT for 10–15 min, shielded from light. After this incubation period, the well plates were turned upside down to ensure proper 3D distribution of cells within the hydrogel, and further incubated at RT for an additional 5–10 min. Subsequently, each well was irradiated the corresponding UV time (from 10 s to 150 s) and washing was performed twice with DG0 to remove the unreacted photoinitiator. Then, DG10 was added to each well. For collagen hydrogels, the same protocol as previously described for GelMA and GelMA–SH was followed unless for the incubation process which occurred inside an incubator at 37 °C instead of RT.

Finally, 96-well plates were cultured for 3 days under standard conditions, with DG10 being exchanged every other day. Three to four cell-laden hydrogels were prepared for each experimental condition.

### Cell viability

Cell viability assessment was conducted on days 1 and 3 of cell culture using a live/dead staining protocol. The cell-laden hydrogels were incubated with 2 μg mL$^{-1}$ of calcein-AM (CAM) and 6 μg mL$^{-1}$ of propidium iodide (PI) in DG10 for 30 min under standard culture conditions. An inverted fluorescence microscope (Leica DMi8) was used to monitor cell viability. The obtained fluorescence images were processed with ImageJ software, and manual thresholding was applied to quantify cell viability. Analysis of HCT-116 cell clusters was performed by randomly selecting 150 clusters of each condition and manually fitting their areas to spheroidal/elliptical shapes.

**Cell metabolic activity.** The metabolic activity of HCT-116 or MIA PaCa-2 cells embedded in the hydrogels was assessed using the 3-(4,5-dimethylthiazol-2-yl)-5-(3-carboxymethoxyphenyl)-2-(4-sulfophenyl)-2*H*-tetrazolium (MTS) reagent. On days 1 and 3 of cell culture, DG10 medium was replaced with 200 μL of fresh DG10 in each well. Subsequently, the cells were incubated at

37 °C with 20 μL of MTS reagent diluted to a final concentration of 9.1% v/v, following the manufacturer's recommendation. After a 4-hour incubation, the resulting colored solution was gently mixed by pipetting, and the absorbance was measured at a wavelength of 490 nm using a microwell plate reader (Multiskan Go, Thermo Scientific). The absorbance of each condition was normalized to the absorbance obtained from cells embedded in collagen hydrogels. For each experimental condition, three replicates were prepared.

### DNA extraction

On days 1 and 3, well plates containing the cell-laden hydrogels were frozen at −80 °C until further use. To prepare for DNA isolation, each hydrogel was finely powdered in liquid nitrogen using a cold mortar and pestle. The collected samples were then processed following the peqGold Blood & Tissue DNA Mini Kit protocol from VWR. Total DNA was isolated and quantified using a Nanodrop spectrophotometer (Synergy HT, BioTek). For DNA quantification, calibration was carried out using solutions with increasing cell concentrations. Cell pellets were treated similarly to the hydrogel samples. For each experimental condition, three samples were tested.

**Cell membrane staining & real-time cell monitoring.** For live cell imaging experiment and prior to the fabrication of cell-laden hydrogels, HCT-116 and MIA PaCa-2 cells were incubated with Cell Tracker Orange CMTMR (final concentration 15 μM) to stain the cell membrane. After 20 min of incubation under standard culture conditions and protected from light, washing with DG0 and centrifugation was performed twice. Then, the cell pellets were resuspended with the corresponding amount of collagen, GelMA or GelMA–SH precursor mixtures to prepare the final embedded hydrogels. The 96-well plate was placed in the IncuCyte® SX5 live-imaging system with a green/orange/NIR optical module and monitored for 3 days. Under the Standard scanning mode, brightfield and orange fluorescence images were acquired with a 20× objective. Acquisition parameters were set at capturing 4 images per well and scanning at intervals of 3 h for a total duration of the experiment of 3 days. Non-adherent cell-by-cell analysis was performed using the IncuCyte® software. For each experimental condition, three samples were tested and calculations were carried out with three thresholded images (one image per replica).

**F-actin and nuclei staining and visualization.** After 3 days of cell culture, cell-laden hydrogels were rinsed with PBS three times and fixed with 4% PFA for 20 min at RT. After washing twice with PBS, samples were stored at 4 °C until further use. For F-actin staining, PBS was removed from wells and hydrogels were transferred to an 8-well μ-slide (Ibidi) and permeabilized with 0.1% v/v Triton X-100 for 20 min at RT. Cell-laden hydrogels were then incubated with Alexa Fluor 488 Phalloidin (1 : 400) for 90 min at RT while protected from light. After rinsing three times with PBS, nuclei staining was performed with DAPI (1 : 1000) for 60 min at RT protected from light. Confocal images were obtained with a 63× oil-immersion objective (confocal Zeiss LSM 880 with a Plan-Apochromat 63X/1.4 oil (DT 0.19), DIC objective).

### Data analysis and statistics

All results are presented as mean ± standard deviation (SD). Graph plotting and statistical analysis were performed using OriginPro 2020 software (OriginLab). Prior to significance testing, normality was assessed using the Shapiro-Wilk test, and the equality of variances between datasets was examined. For determining significant differences ($p < 0.05$), Student's *t*-tests and one-way ANOVAs with Tukey's *post hoc* tests were employed.

## Results and discussion

### Functionalization of gelatin

The methacrylation of gelatin is a commonly employed technique to produce photocrosslinkable derivatives, facilitating the creation of a chemically bonded network upon exposure to UV light. In the present work, the method described by Shirahama *et al.*[26] was utilized to adjust the experimental parameters and optimize the incorporation of methacryloyl groups into gelatin as previously described.[17] Successful methacrylation of primary amines present in lysine and hydroxylysine residues was confirmed using $^1$H-NMR spectroscopy[30] (Fig. S1, ESI†). The signals at 5.4 and 5.7 ppm, corresponding to the vinyl protons, and the peak at 1.9 ppm, attributed to the methyl groups, provided evidence of the presence of methacrylamide groups. Additionally, the characteristic lysine signal at 3.0 ppm almost vanished in the GelMA spectra, indicating the reaction of the ε-amino groups with MAA. The TNBS assay results indicated an 85% yield in the transformation of free amines to methacrylamide groups. Notably, this reaction does not involve arginine residues, ensuring that the RGD motifs remained intact, and GelMA retained its favorable cell adhesive properties.[32]

### Preparation and mechanical characterization of cell-free hydrogels

As described in our previous work,[17] GelMA and GelMA–SH hydrogels constitute an excellent bioscaffolding platform for *in vitro* cellular studies with epithelial cells. Given the good results obtained, the present study was conducted using the same hydrogels for 3D *in vitro* cell culture studies. We decided to keep most of the experimental parameters, such as the photoinitiator system I2959 and the GelMA concentration (6% w/v), since previous studies in the literature had already demonstrated good cell viability[33] and biocompatibility.[34]

Taking into account the ultimate 3D *in vitro* cell culture experiments and the fact that the aqueous media used in photopolymerization strongly influences the mechanical properties of hydrogels,[35] all gelatin derivative and collagen solutions were prepared in DG0. In the case of gelatin-based precursor mixtures, they were poured into PDMS molds and kept at RT, shielded from light, for 20 min before UV irradiation, leading to the formation of a physical gel. As time progresses, the random coil GelMA chains come together and form triple helices through hydrogen bonds, leading to the process of physical gelation (Fig. 1).[36] This physical gel

 

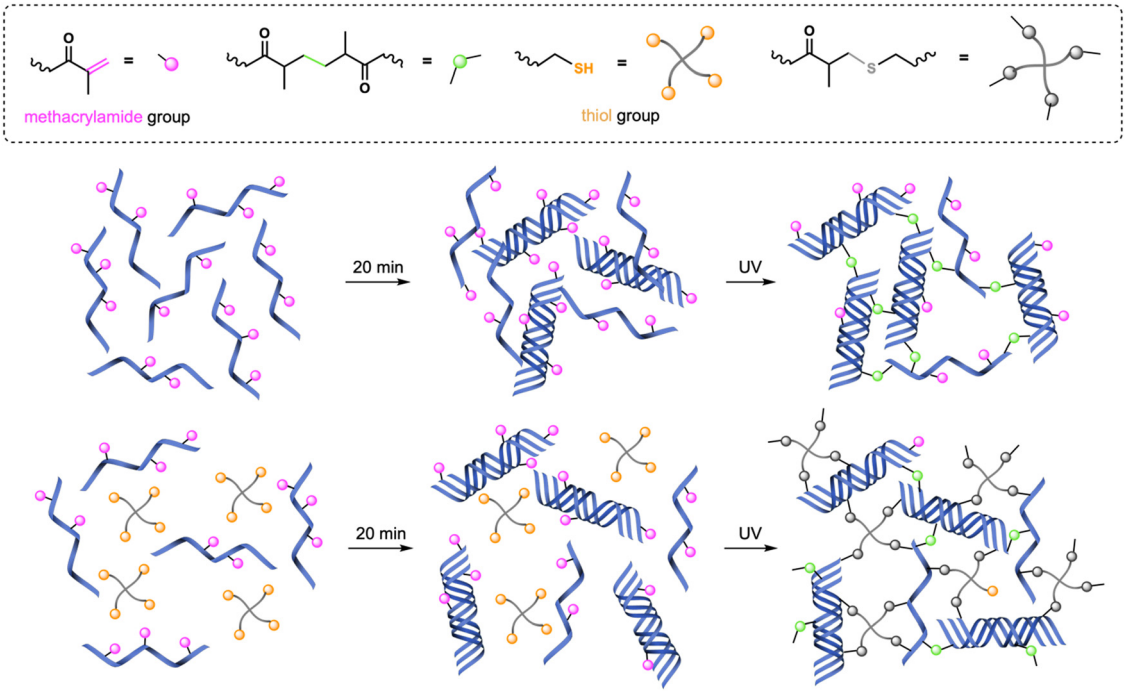


Fig. 1 Crosslinking procedures for GelMA and GelMA–SH hydrogels. Physical gelation at RT takes place during the 20 min incubation period.

formation taking place before UV irradiation is known to yield stiffer networks with enhanced mechanical properties.[37]

Consequently, after the 20-min period incubation at RT, GelMA hydrogels were fabricated following a chain-growth mechanism[38] by exposing the precursor mixture to actinic light for 30 s or 150 s (named as GelMA-30 and GelMA-150, respectively). Regarding GelMA–SH hydrogels, the introduction of thiol-methacrylamide chemistry enabled a mixed-mode crosslinking upon UV irradiation (chain-growth and step-growth mechanisms) which is related to higher conversion of functional groups.[39] This higher conversion has been previously demonstrated to lead to stiffer hydrogels by using GelMA in combination with the 4-arm thiol also employed in this work. That is, keeping the same UV dose for curing, GelMA–SH hydrogels are stiffer than their GelMA analogues.[17] We have applied this alternative mixed-mode crosslinking strategy to fabricate two different GelMA–SH hydrogels. Following a similar preparation method that that used in GelMA hydrogels, after the incubation period, we have employed two different UV light doses: 10 s and 30 s for hydrogels named SH-10 and SH-30, respectively. It is worth to mention that GelMA–SH hydrogels were prepared at a methacrylamide : thiol ratio of 1 : 0.5 (6% w/v GelMA and 1% w/v 4-arm thiol) to achieve a good balance between the double bonds and sulfhydryl nucleophiles, preventing dangling structures caused by an excessive thiol proportion.[40]

We decided not to dissolve the photoinitiator I2959 in methanol since cells embedded within the network would be affected by the presence of the organic solvent.[41] This choice was grounded in a preliminary assay carried out with GelMA-150 hydrogels encapsulating HCT-116 cells prepared by keeping or removing the methanol from the precursor mixture preparation protocol. As shown in Fig. S2 (ESI†), cell toxicity was considerably reduced (55-fold) in hydrogels without methanol. Consequently, all gelatin derivative solutions were prepared by just thoroughly dissolving I2959 together with GelMA macromer in warm DG0.

Additionally, to compare cell behavior against a 3D control network, collagen hydrogels were fabricated. The vast majority of articles on collagen hydrogels work at concentrations lower than 4 mg $mL^{-1}$[42,43] which constitute a lower collagen content than that of native tissue. Cancerous tissue presents a variable collagen concentration ranging from 9 to 45 mg $mL^{-1}$,[44] however, the high viscosity of the precursor mixtures complicates the experimental process. For this reason, we decided to increase the collagen concentration compared to most of the works published in the literature to approach a more physiological content. Thus, the collagen hydrogels in this study were prepared at 6 mg $mL^{-1}$. As described in the previous section, the collagen precursor mixture was prepared in DG0, poured into PDMS molds and incubated at 37 °C the same 20-min period time than GelMA-based hydrogels. During this time, self-assembly of collagen molecules takes place rapidly to generate a consistent scaffold.[42] Apart from these widely prepared collagen hydrogels (named as "Col" throughout the manuscript) and to also include the UV light parameter into the control samples, we decided to irradiate some of the collagen hydrogels with the highest UV time among all conditions, that is, 150 s (named as Col-150). Thus, the following mechanical and biological discussion is focused on six different bioscaffolds varying the network crosslinking procedure and the UV-exposure time: Col-0, Col-150, GelMA-30,

GelMA-150, SH-10 and SH-30 (photocrosslinked cell-free hydrogel images are shown in Fig. S3, ESI†).

**Mechanical testing: AFM.** The mechanical characterization of the hydrogels started with nanoindentation measurements to obtain the Young's Moduli. Although bulk measurements offer a comprehensive view of the 3D cell culture environment, the increasing acknowledgment of the crucial role of matrix stiffness at the microscale in influencing cell functions[45,46] has launched the AFM technique to become a widespread application to determine local gel mechanics.[47] In fact, a thorough study was recently performed by Richbourg *et al.*[48] who cross-evaluated five measurement methods of stiffness in covalently crosslinked PVA hydrogels. According to these authors, conducting multiple distributed nanoindentation experiments can verify the uniformity of the entire sample and indeed, they found that nanoscale stiffness generally aligned with macroscale stiffness in PVA hydrogels, showing no consistent deviation.

To create the closest physiologically relevant environment possible, crosslinked hydrogels were allowed to reach equilibrium swelling at standard culture conditions before nanoindentation. After 24 h of swelling, AFM measurements were conducted in DG0 at 37 °C (Fig. 2).

Physically crosslinked collagen control hydrogels (Col-0) exhibited a Young's Modulus of 1.1 kPa. This result is in good agreement with several studies in the literature which have reported stiffness in the range 0.5–2 kPa, for collagen hydrogel scaffolds formed under similar collagen concentration and polymerization temperature.[43,49] The irradiation with 150 s of UV light yielded to stiffer hydrogels with a Young's Modulus of 2.1 kPa. This UV-derived hardening mechanism has been previously observed for collagen hydrogels. Ishibashi *et al.* recently reported that the storage modulus for pre-gel collagen solutions increased with the UV dose.[50] Maeda analyzed the effect of different UV wavelengths in the mechanical properties of collagen gels *in vitro*.[51] This study confirmed that tyrosine crosslinks (dityrosines) increased with radiation at wavelengths between 300–340 nm, having the radiation at 330 nm the greatest effect. Despite the fact that the maximum emission peak from our UV lamp is 365 nm, the equipment covers a wavelength range from 320 to 390 nm. The shortest wavelengths emitted by our lamp could cause dityrosine formation contributing to the observed stiffening of collagen hydrogels.

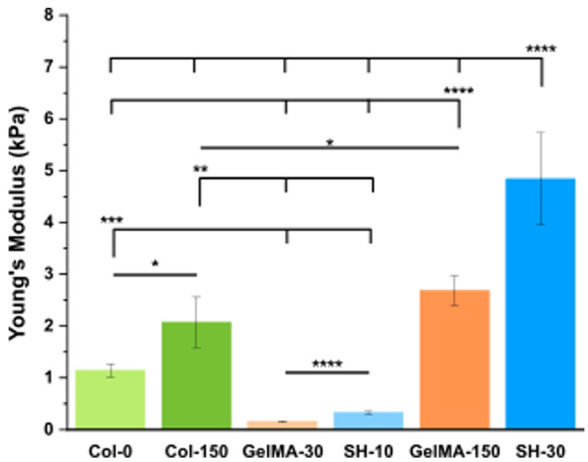


Fig. 2 Stiffness results for collagen, GelMA and GelMA–SH hydrogels prepared in DG0 after different UV exposure times. Error bars SD. Note: ****$p < 0.0001$, ***$p < 0.001$, **$p < 0.01$, *$p < 0.05$.

Free radical crosslinked GelMA scaffolds were prepared by irradiating with UV light for 30 s or 150 s (referred to as GelMA-30 and GelMA-150, respectively). The Young's Modulus obtained for GelMA-150 was 2.7 kPa, almost 17 times higher than GelMA-30, that was 0.16 kPa. Comparison between GelMA–SH hydrogels yielded a similar rise of approximately 15 times from SH-10 (0.33 kPa) to SH-30 (4.8 kPa). As previously reported for homologous pre-hydrogels generated using methanol to facilitate the photoinitiator solubilization, both chemistries allow to tune the stiffness of the hydrogel over a large range of values with biological interest, however the SH hydrogels lead to similar values with much lower UV doses, when compared with GelMA scaffolds.

Interestingly, comparing these results with the ones obtained for hydrogels formulated with methanol (Fig. S4A, ESI†), an almost identical stiffness trend was observed, increasing in the following order: GelMA-30, SH-10, GelMA-150 and SH-30.[17] Nevertheless, a notable aspect was that all gelatin-based formulations without methanol yielded softer hydrogels. Besides, the shorter the UV exposure time applied, the greater the decrease in stiffness with respect the methanol-containing formulations. SH-10, GelMA-30, SH-30 and GelMA-150 underwent a 9-fold, 7-fold, 4.5-fold and 2-fold reduction in Young's Moduli. To elucidate a feasible explanation, it seems obvious the key role of methanol in properly dissolving the photoinitiator I2959. In general, one of the main requirements of photonitiators is a good solubility in the precursor solution.[52] The efficiency of the derived photochemical processes is strongly influenced by the efficiency of the photoinitiator generating radicals. We assume that removing methanol from the fabrication protocol led to a poor solubility of I2959 in the cell culture medium DG0 and consequently to a lower crosslinking degree in all cases. Additionally, methanol could also have a role in the physical gelation taking place while incubation at RT. As described above, at the initial stage of gelation, random coil GelMA chains aggregate through hydrogen bonding. The presence of methanol in the precursor mixture could promote structural stability owing to the enhanced intramolecular bonding.[53]

Diseased tissue typically exhibits higher stiffness than healthy tissue. Several studies have confirmed that normal tissues present Young's Moduli around 1 kPa for both healthy colon[54,55] and pancreas.[3,43] In contrast, colorectal cancer tissue exhibits variations in stiffness based on the degree of disease progression[54] and pancreatic cancer tissue is characterized by a heterogeneous map of stiffness as a result of fibrosis.[3] Nebuloni *et al.* performed AFM measurements with CRC samples derived from three donors and found that the vast majority of results ranged from ~3 to ~30 kPa.[55] The median elastic modulus obtained by Kawano and coworkers for CRC samples

 

from 106 tissue donors was 7.51 kPa but the whole range covered from 1.1 to 68.0 kPa.[54] As for human pancreatic tumors, Rubiano *et al.* employed a custom indentation equipment to test the resected samples, reporting a mean value of 5.46 ± 3.18 kPa[43] while Rice and coworkers showed an upper quartile mean stiffness of 4 kPa for PDAC.[3] Considering our platform of hydrogels and the Young's Moduli obtained, GelMA-30 (0.16 kPa) and SH-10 (0.33 kPa) scaffolds would be even softer than healthy tissue. On the other hand, Col-0 (1.1 kPa), Col-150 (2.1 kPa), GelMA-150 (2.7 kPa) and SH-30 (4.8 kPa) hydrogels showed stiffness matching with the initial stages of CRC but also with the metastatic tumors and the highly fibrotic PDAC stroma.

As a conclusion for this section, a precise control over stiffness with remarkable reproducibility led to the preparation of custom-tailored hydrogels upon well-defined and easily-adjustable irradiation UV times. The mechanical properties of the prepared hydrogels closely resemble those of both healthy and tumoral pancreas or colon tissues, making them a promising platform for cancer research.

**Gel fraction and swelling properties.** As shown in Fig. 3(A) there was no significant difference between the gel fractions of Col-0 and Col-150 hydrogels with values near 30% in both cases. Col-150 exhibited higher stiffness than the non-irradiated control but as it has already been explained, this could be due to the formation of dityrosine crosslinks. Since type I collagen is a triple-helical protein, it is highly likely that dityrosine crosslinking takes place between tyrosine residues from adjacent polypeptide chains within the helix or even intramolecularly. This condition would reinforce the collagen network in terms of stiffness not affecting the total solid content. The comparison of Col-0 and Col-150 with gelatin-based scaffolds has been discarded since the latter are chemically crosslinked scaffolds (while collagen hydrogels are prepared only by physical gelation) and in addition, the initial solid content in the precursor formulations varies one order of magnitude (6 mg $mL^{-1}$ in collagen mixtures and 60 mg $mL^{-1}$ in gelatin-based mixtures).

Considering the definition of gel fraction, this property indicates the percentage of macromer molecules forming the 3D network. It is hence expected that the softest hydrogels with low degrees of crosslinking (GelMA-30 and SH-10) exhibit also low values of gel fraction (15.1 ± 1.5% and 29.6 ± 6.3%, respectively) as a result of a higher proportion of non-bounded polymer chains leaching out from the network during swelling. In contrast, the stiffest scaffolds (GelMA-150 and SH-30) displayed higher gel fractions (74.6 ± 2.9% and 70.4 ± 1.1%, respectively) according to also higher final polymer concentrations. These results agree with the works of several authors for related materials.[34,56] Notably, even though the gel fraction outcomes are almost identical, SH-30 scaffolds exhibited a significantly higher stiffness (4.8 kPa) than GelMA-150 (2.7 kPa) as described in the section above. Again, this result is originated by the thiol click chemistry: a mixed-mode crosslinking strategy comprised a larger amount of reactive groups, yielding a higher crosslinking density and stiffness.

As for the swelling properties (Fig. 3(B)), Col-0 and Col-150 hydrogels exhibited no significant differences in their elevated mass swelling ratios (34.4 ± 1.9 and 38.0 ± 1.3, respectively). Indeed, it is known that collagen stands out for its exceptional degree of hydration which plays a crucial role in the stabilization of the triple helical conformation.[57] Interestingly, in a very similar manner as the comparison described in the previous section, MSR results displayed the same trend as the one obtained for methanol-containing GelMA-derived hydrogels (Fig. S4B, ESI†), although absolute values were higher in all cases (matching with the lower stiffness). Less crosslinked hydrogels, which are softer, exhibit higher capacity to absorb aqueous medium. This was confirmed by comparing pairs of scaffolds created through the same synthesis strategy: GelMA-30 (MSR: 26.9 ± 1.5) demonstrated a 1.8-fold increase compared to GelMA-150 (MSR: 14.7 ± 0.1). Likewise, SH-10 scaffolds (MSR: 40.8 ± 4.9) were characterized by a 1.6-fold higher MSR than SH-30 (24.8 ± 0.6). However, the comparison between the two softest hydrogels showed an inverse trend: SH-10 condition exhibited an unexpectedly high MSR compared to

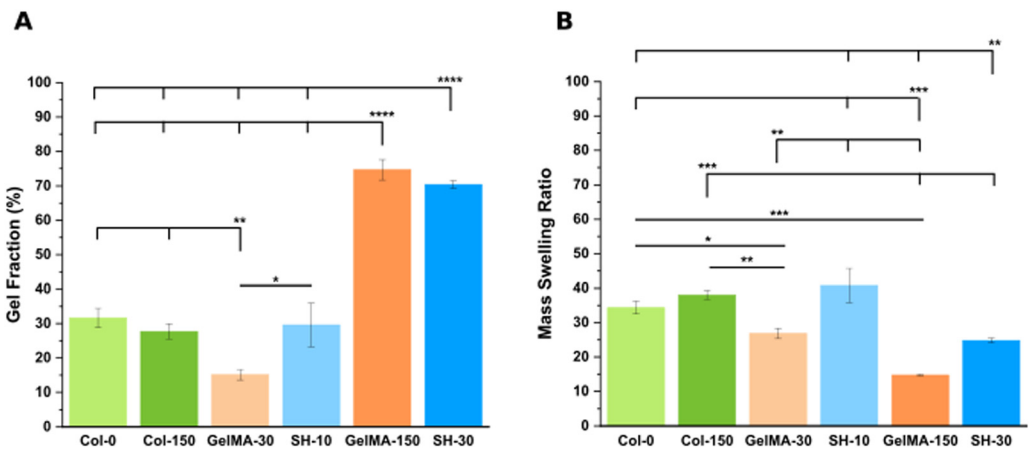


Fig. 3 Swelling characterization in DG0: gel fraction (A) and mass swelling ratio data (B). Error bars SD. Note: ****$p < 0.0001$, ***$p < 0.001$, **$p < 0.01$, *$p < 0.05$. Non-statistical differences are not drawn in the graph.

GelMA-30 (1.5-fold increase) while it was also twice as stiff. Similarly, SH-30 displayed a 1.7-fold rise in MSR than GelMA-150 whereas stiffness was 1.8 times higher. This increased swelling capacity is attributed to the presence of hydrophilic PEG-thiol chains in the GelMA–SH networks. Additionally, Bertlein *et al.*[34] explained the different swelling behavior depending on the network crosslinking mechanism. Free radical photopolymerization is associated to heterogeneous networks[58,59] with reduced swelling capacity. In contrast, hydrogels fabricated through thiol click chemistry are defined by a more uniform distribution of crosslinking density with enhanced swelling properties.

Summing up, the comparison between GelMA-based scaffolds fabricated through the same chemical crosslinking mechanism (either chain-growth or mixed-mode photopolymerization) confirmed that softer hydrogels displayed lower values of gel fraction and hence, greater MSR values. In addition, the introduction of the PEG chains within the hydrogel network led to a remarkable rise in the swelling capacity.

## Cell culture

**Cell growth and proliferation.** Homologous hydrogels have been previously used as substrates where epithelial cells were seeded on top, creating semi-3D models with good cell proliferation rates and forming a confluent monolayer of polarized Caco-2 cells.[17] Considering the favorable biological behavior of the hydrogel materials, we aimed to further exploit the potential of this material platform by transitioning to 3D models with cells embedded within the hydrogels. While Caco-2 cells are primarily employed for mimicking the intestinal barrier according to their well-known behavior of establishing a polarized cell monolayer, for three-dimensional studies we have selected HCT-116 cells representing the colorectal cancer condition[22,60] and MIA PaCa-2 cells for the pancreatic disease.[25] Tumoral cells were encapsulated within the six aforementioned types of hydrogels – Col-0, Col-150, GelMA-30, GelMA-150, SH-10 and SH-30 – and cultured for 3 days. Cell viability was assessed using CAM/PI staining at day 1 and day 3. Since cells were present during the UV-crosslinking, Col-150 was used to assess the effect of UV irradiation on cell viability. As shown in Fig. 4 all matrices exhibited an excellent cytocompatibility for HCT-116 cells with only a slightly higher mortality in GelMA-150 hydrogels at day 1. At first glance, one could think about the UV light dose of 150 s generating this difference in cell behavior, however, Col-150 condition displayed the same extremely low mortality as the other hydrogels. Taking it all together, we hypothesize about a synergistic effect of the large UV irradiation time and the simultaneous crosslinking of GelMA chains. We have assessed this influence of UV irradiation on cell viability only in collagen samples, since unlike collagen, GelMA chains need to be UV-irradiated to form an irreversible crosslinked network and it is not possible to have GelMA-0 hydrogels.

On the other hand, considering the area occupied by living cells (green area in live/dead micrographs), it seems that both GelMA scaffolds presented the highest composition affinity towards HCT-116 cells with CAM areas around 50% while the living cell occupancy for the other four scaffolds was near 40% (Fig. 5(A)).

Interestingly, the initial single cell suspension of HCT-116 cells underwent proliferation, resulting in all cases, in the formation of compact cell clusters throughout the 3-day experimental period with particularly distinct features depending on the hydrogel (Fig. 6). In order to gain insight in the cell cluster formation, we sorted the cluster in three groups attending to their size: clusters with areas below 500 $\mu m^2$, in the range of 500–1000 $\mu m^2$ or larger than 1000 $\mu m^2$ were defined as ''small'', ''medium'' and ''large'', respectively (Fig. S5, ESI†). On one hand, Col-0 and Col-150 hydrogels exhibited the most homogeneous distributions in terms of cluster sizes, although a higher amount of medium (blue) and large (yellow) structures were observed rather than small ones (pink). In GelMA-30, the softest biomaterial in this study, there was a clear predominance of large clusters, being the cell area occupied by this type of aggregates (32.1%) the highest among all scaffolds. Notably, medium cell aggregates had a very low occupancy (3.4%), almost 4 times less than the smallest clusters (12.7%). On the other hand, the cell area occupied in GelMA-150 hydrogels, which showed the nearest stiffness to Col-0 and Col-150, was equally distributed among the three sizes of clusters, as well. Similar to GelMA-30, the also soft SH-10 condition promoted an area occupancy dominated by the larger clusters (20.0%) while medium and small structures occupied a similar area (7.8% and 7.1%, respectively). Finally, the stiffest hydrogel SH-30 area was also evenly occupied by large, medium and small clusters although it is worth mentioning that this condition displayed the lowest occupancy by large clusters (10.2%) among the six hydrogels. Looking at each pair of hydrogels with the same chemical composition (Col, GelMA and SH), it is clear the effect of stiffness on the aggregates size: the higher area occupied by large clusters was observed when HCT-116 cells were cultured in the softer hydrogels. Our results agree with other works found in the literature on epithelial breast cancer and ovarian cancer where larger cell aggregates presented a progressively lower area occupancy with increasing stiffness.[61–63] This could be explained by the degree of restriction established by the matrix: low-stiffness hydrogels offer a permissive environment for cell migration and growth. In contrast, high-stiffness hydrogels correspond to matrices that may restrict cell cluster growth. Above all, it should be highlighted that these 3D cellular structures emerged without the need for any biochemical stimuli, showcasing the adaptability of collagen and GelMA in creating a tunable biomimetic tumor microenvironment. Histograms and visual scheme on cluster size quantification are shown in Fig. S5 (ESI†). Finally, and as a consequence of cellular clustering, CAM areas at day 3 decreased in all cases, being especially significant in the stiffest conditions: GelMA-150 and SH-30 (Fig. 5(A)).

Regarding MIA PaCa-2 cell line, a non-aggregating pattern was observed and all scaffolds showed excellent biocompatibility at days 1 and 3 (Fig. 4). In addition, cells quickly proliferated and CAM areas increased from 35–40% (day 1)

 

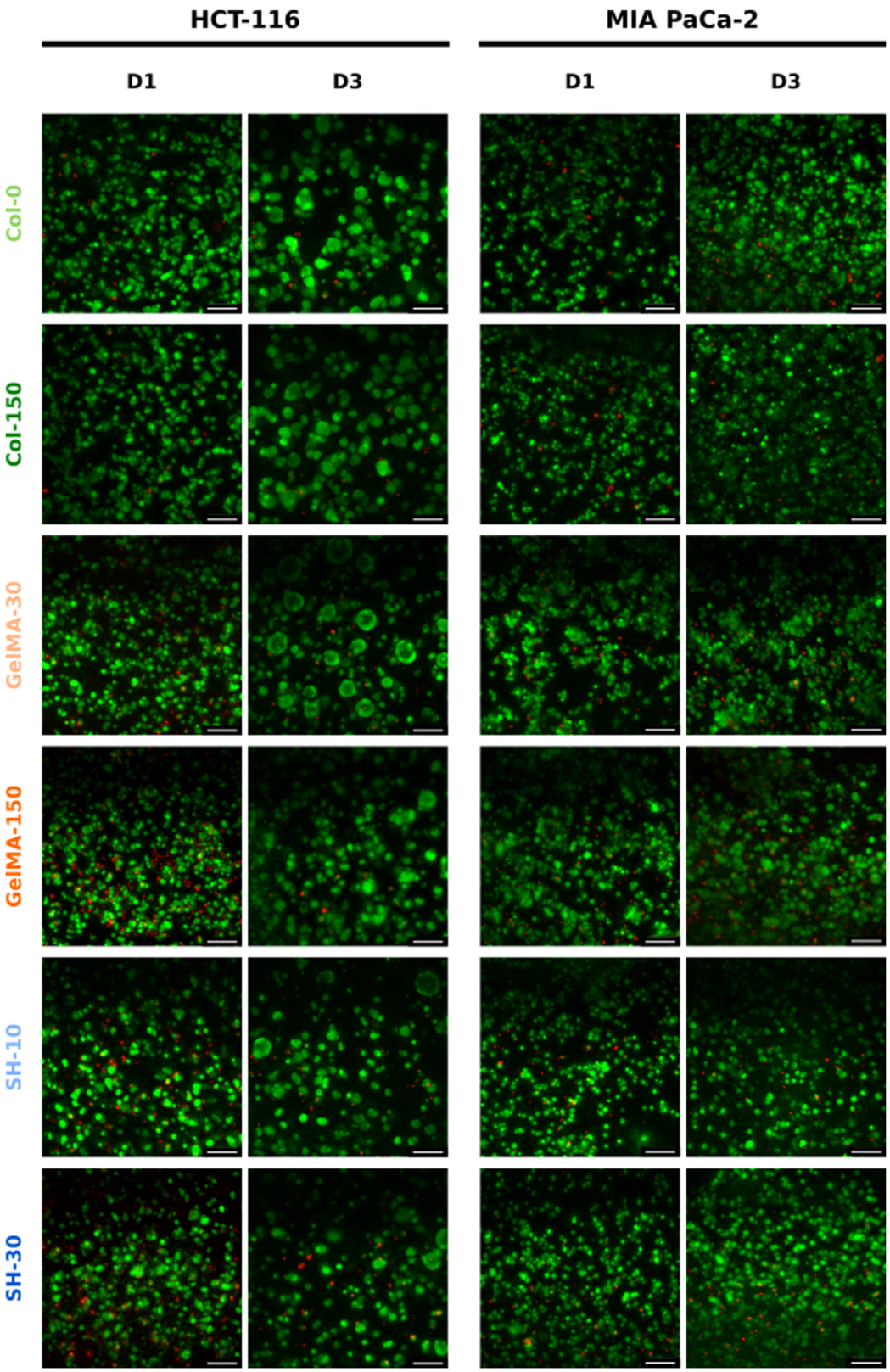


Fig. 4 3D culture of HCT-116 and MIA PaCa-2 cells embedded within collagen and GelMA-based hydrogels over 3 days. Live/dead micrographs of HCT-116 (left) and MIA PaCa-2 cells (right) evolution on Col-0, Col-150, GelMA-30, SH-10, GelMA-150 and SH-30 scaffolds on day-1 and day-3 of cell culture. The scale bar represents 100 μm for 20× micrographs.

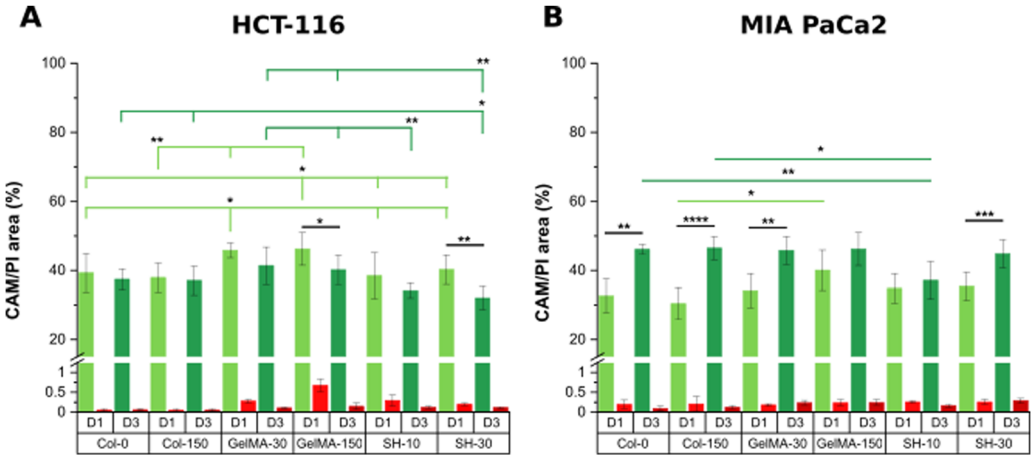


Fig. 5 Area percentage of alive CAM (green) and dead PI (red) stained cells from micrographs of HCT-116 (A) and MIA PaCa-2 cells (B) on collagen and GelMA-based scaffolds on day-1 and day-3 of cell culture. Error bars SD. Note: ****$p < 0.0001$, ***$p < 0.001$, **$p < 0.01$, *$p < 0.05$ (non-statistical differences are not drawn in the graph).

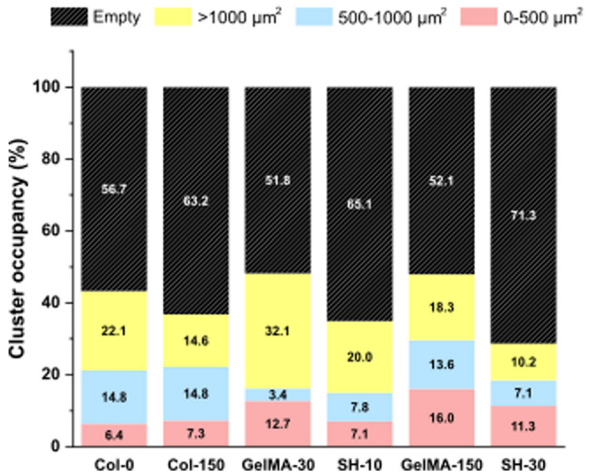


Fig. 6 HCT-116 cluster occupancy percentage from CAM staining in live/dead micrographs at day 3 of 200 × 200 μm (20× objective) in collagen and GelMA-based hydrogels depending on the cluster size. Small, medium and large clusters are represented in pink, blue and yellow, respectively.

up to near 50% (day 3) in all cases, with the exception of SH-10 (Fig. 5(B)). Conversely to HCT-116, matrix stiffness and composition did not apparently affect biological behavior in terms of cell growth and morphology.

To sum up, the platform of bioscaffolds generated to encapsulate HCT-116 and MIA PaCa-2 cells yielded physiologically relevant matrices where cells remained viable, grew and successfully proliferated (3D renders of the three-dimensional distribution of cells within the hydrogels are shown in Fig. S6, ESI†).

**Live-cell time-lapse imaging.** To gain a deeper knowledge about cell growth and also cell clustering in the case of HCT-116 cells, real-time cell proliferation was monitored using the IncuCyte® system. With this equipment, it becomes possible to perform live imaging of cell-laden hydrogels without the need to remove the cell culture plate from the incubator. Cell membrane was stained with the fluorescent dye Cell Tracker Orange CMTMR and the real-time screening was conducted for 3 days, scanning at intervals of 3 h. As shown in Fig. 7, clear and defined cellular shapes were only imaged in the softer hydrogels GelMA-30 and SH-10 due to their loose networks. Phase confluence analysis was conducted for all six conditions, however, we herein discuss the most reliable results corresponding to GelMA-30 and SH-10. According to Fig. S7 (ESI†), HCT-116 cells showed a generally higher occupancy in GelMA-30 than in SH-10 as already seen with live/dead images although cell area occupancy did not considerably vary throughout the experimental period in none of the conditions. Likewise, phase area occupancy in MIA PaCa-2-laden hydrogels hardly displayed differences among the six hydrogels (Fig. S7, ESI†).

The truly appealing feature of HCT-116 cells to be analyzed with the Incucyte® system was the cluster-like conformation observed in all scaffolds. The progressive formation of these 3D cellular aggregates was easily followed in the softest hydrogels GelMA-30 and SH-10. Time-lapse movies can be found in the ESI.† As confirmed in Movies 1 and 2, (ESI†) cells started to move within the network and group together from the very beginning. Individual migration of single cells was observed according to Fig. S8 (ESI†). Small multicellular clusters were already observed after 17 h of cell culture both in GelMA-30 and SH-10 hydrogels and kept growing over time not only because of cell proliferation but also the assembly of cell aggregates that were initially separated in close proximity and moved toward each other progressively. Upon coalescence, the newly formed cluster undergoes a remodeling and compacting event, matching with the results reported by Palmiero *et al.* with several cell lines in their study about collective directional migration.[64] Furthermore, during the experimental process, cell aggregates had the ability to rotate within the crosslinked network as shown in Fig. S9 (ESI†). This event was also reported by Peela *et al.* in their developed tumor model for breast cancer with

 

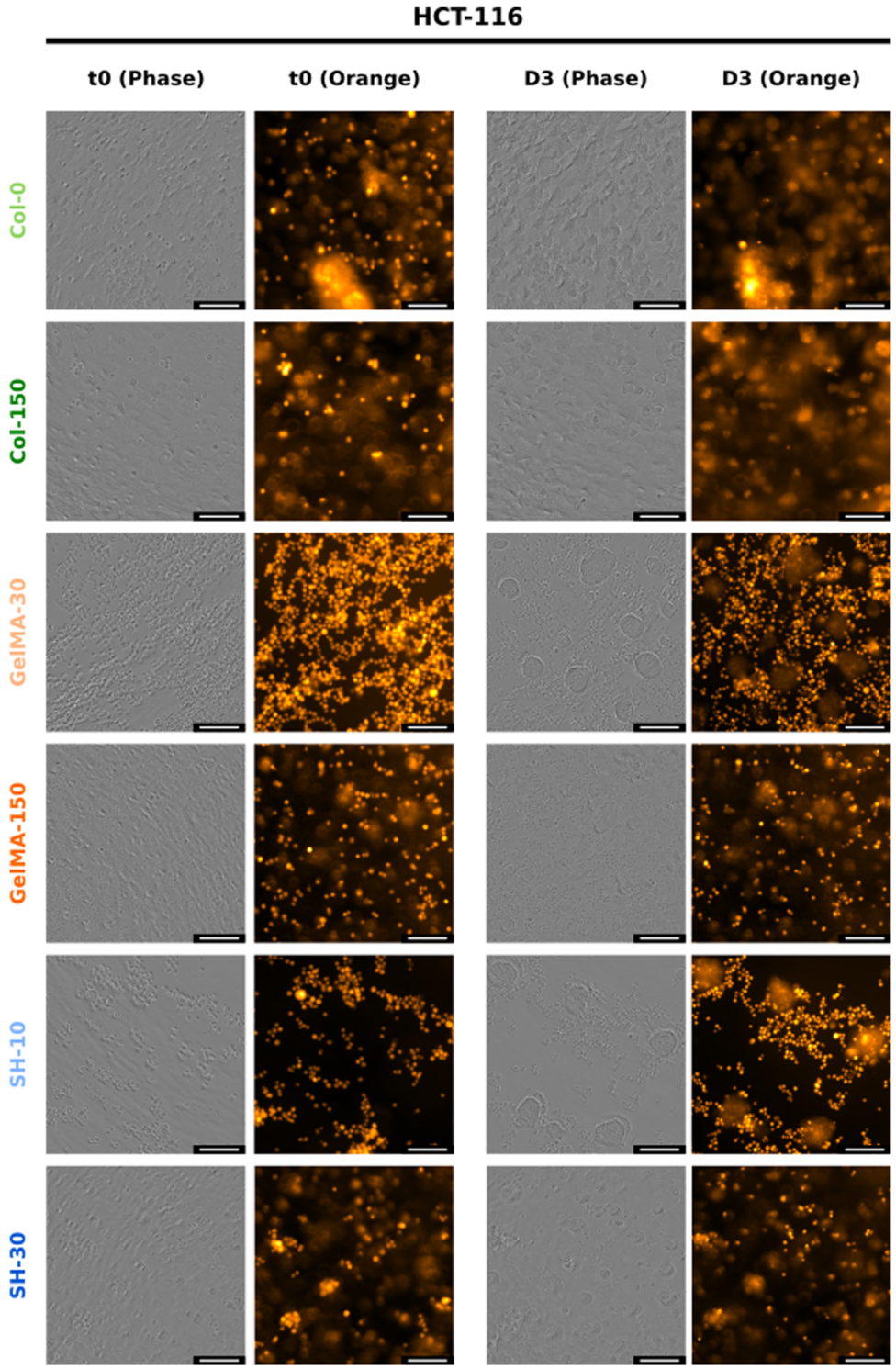


Fig. 7 Phase-contrast and orange fluorescence images from IncuCyte® of HCT-116-embedded hydrogels at $t$ = 0 (left) and day-3 (right). The scale bar represents 100 μm for 20× micrographs. (The twin figure for MIA PaCa-2 cells corresponds to Fig. S12, ESI†).

MCF7 and MCF10A clusters formed in GelMA hydrogels.[9] Likewise, Tanner and coworkers thoroughly described cellular rotation during the formation of glandular tissue and proposed this phenomenon to be promoted by the temporal loss of cell–ECM interactions and local degradation of ECM.[65] As mentioned above, we additionally observed how clusters approximated to each other to finally assemble into a larger aggregate (Fig. S10, ESI†), probably due to the secretion of autocrine and paracrine factors that can modulate and drive the migration of the surrounding cells. In this respect, a wealth

of studies has focused on collective cell migration taking place during metastasis. Although several phenomena remain to be investigated, there is evidence that tumor cell communication is supported by the expression of cell adhesion molecules such as E-cadherin (essential for adherent junctions)[66] and mediated by upstream signaling. The autocrine secretion of soluble factors such as chemoattractants are partly responsible of cluster-cluster crosstalk at distance and collective directional migration occurs due to chemotaxis (concentration gradients).[64,66] Regarding MIA PaCa-2 cell line, we also witnessed cell migration as a function of time, however and conversely to HCT-116 cells, MIA PaCa-2 cells grouped together while keeping intact their membranes as well as the fluorescence, not fusing into 3D clusters (Fig. S11, ESI†).

Thus, real-time cell monitoring disclosed individual and collective cell migration of both HCT-116 and MIA PaCa-2 cells. Notably, it was observed that the progressive approach between HCT-116 cells along with cell proliferation generated well-defined clusters with the ability to rotate and migrate.

**Motility structures: actin-based protrusions.** In order to confirm that the observed HCT-116 migratory behavior correlated with the expression of motility structures, F-actin in the cytoskeleton was analyzed through phalloidin staining in cells embedded within GelMA-30 (softest condition) and SH-30 hydrogels (stiffest condition). Both HCT-116 individual cells and clusters exhibited a rounded shape with a defined cortical F-actin ring (Fig. 8). Remarkably, actin-based protrusions known as filopodia were observed at the cell margins, which are likely associated with cell migration processes.[67,68] Filopodia are long and slender dynamic structures which can rapidly extend and retract in multiple orientations, enabling cells to perceive their microenvironment and establish connections with neighboring cells or surfaces.[69] Thus, the presence of filopodia on the surface of HCT-116 cells allow them to sense chemical cues eventually promoting cell motility.

**Metabolic activity.** MTS assay was conducted to quantitatively determine the metabolic activity of the proliferating cells encapsulated within the hydrogels. All results were normalized to the Col-0 hydrogel control at day 1. Metabolic activity of HCT-116 cells (Fig. 9(A)) embedded in Col-0 and Col-150 scaffolds was not affected by the culture time nor matrix stiffness. As for the GelMA-based hydrogels, a clear trend was observed: cells embedded in softer hydrogels (GelMA-30 and SH-10) reduced their metabolic activity after 3 days of culture while the stiffer scaffolds promoted the opposite effect, cells encapsulated in GelMA-150 and SH-30 displayed an increase in metabolic activity. This result aligns with the work of Baker and co-authors who found that increased colorectal tissue stiffness resulted in a more proliferative and invasive phenotype.[70] Probably due to differences in the macromer composition, HCT-116 cells embedded in GelMA-based hydrogels were less metabolically active than those in collagen-based scaffolds. According to literature, RGD sequences are known to mediate cell attachment on gelatin scaffolds due to the unfolded structure of gelatin chains and the availability of RGD motifs to bind integrins. However, in the native helical collagen fibers, these motifs are so constrained that they cannot longer interact with integrins and collagen recognition relies on another binding site known as GFOGER. Consequently, integrins involved in cell attachment are different in collagen and gelatin scaffolds.[71,72] Considering the well-described reciprocal regulation of integrins and cell metabolism,[73] this could explain the different metabolic activity recorded for collagen-based and GelMA-based scaffolds.

On the other hand, MIA PaCa-2 cells exhibited a slightly different behavior compared to HCT-116 cell line (Fig. 9(B)). Looking at the soft and medium stiffness hydrogels, Col-150, GelMA-30 and SH-10 exhibited an increased metabolic activity compared to the control Col-0 hydrogel. Although I2959 photoinitiator system has demonstrated excellent cytocompatibility, the irradiation with UV light may cause weak cell damage and as a result, MIA PaCa-2 cells might have become metabolically more active to overcome this initial harm. Similar findings were reported by Kremslehner and colleagues, who found a glucose 6-phosphate dehydrogenase (G6PD) upregulation in keratinocytes as an immediate UV response. G6PD constitutes the initial stage in the metabolic pathway for processing glucose *via* the oxidative branch of the pentose phosphate pathway (PPP). Cells that have previously experienced UV-induced oxidative stress and DNA damage generally exhibit a heightened demand for the products generated by the PPP. Thus, the authors verified that G6PD activity was upregulated in keratinocytes exposed to UV and that this enzymatic activity was increased in cells which initiated nucleotide damage response mechanisms.[74]

Remarkably, all scaffolds with stiffness below 2 kPa (Col-0, Col-150, GelMA-30 and SH-10) displayed a drastic decrease in metabolic activity after 3 days of culture despite the increased live cell area occupancy observed in live/dead micrographs. In contrast, no significant differences were found in GelMA-150 condition at days 1 and 3 while cells encapsulated within the stiffest hydrogel SH-30 showed a slightly higher metabolic activity over time.

In conclusion, the microenvironment created by the softest GelMA-based scaffolds (GelMA-30 and SH-10) promoted a decreased cell metabolic activity for both tumoral cell lines

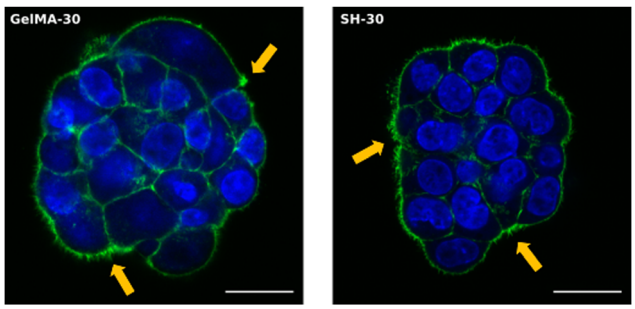


Fig. 8 Expression of F-actin in HCT-116 cells embedded within GelMA-30 (left) and SH-30 (right) hydrogels. Nuclei (blue) and F-actin filaments (green) were stained using DAPI and Alexa Fluor-488 Phalloidin, respectively. Orange arrows indicate filopodia projections in *Z*-stack images. The scale bar represents 20 μm for 63× micrographs.

 

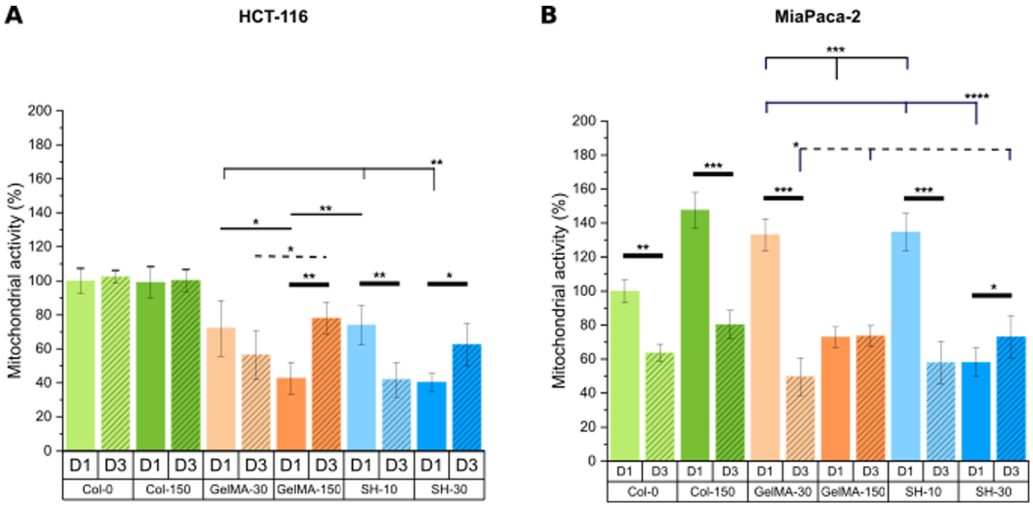


Fig. 9 Mitochondrial metabolic activity was assessed through MTS assay on day-1 and day-3 of cell culture for HCT-116-laden (A) and MIA PaCa-2-laden (B) hydrogels. Error bars SD. Note: ****$p < 0.0001$, ***$p < 0.001$, **$p < 0.01$, *$p < 0.05$. Thin and dashed lines represent statistics among scaffolds on day-1 and day-3, respectively. Thick lines correspond to statistical differences between day-1 and day-3 within the same condition. (Statistical differences towards Col-0 and Col-150 and non-statistical differences are not drawn in the graph – see Fig. S13, ESI†).

HCT-116 and MIA PaCa-2, according to healthy tissue-like conditions. Instead, stiffer GelMA-150 and SH-30 hydrogels markedly generated a rise in HCT-116 metabolic activity while they had minimal effect on MIA PaCa-2 cells.

**DNA content.** Since metabolic activity is not a univocal measurement of cell proliferation, the number of cells present in each hydrogel was determined through the DNA quantification assay. On the one hand, HCT-116 outcomes led to significant differences between days 1 and 3 for SH-10 and SH-30 scaffolds (Fig. 10(A)). Matching with the metabolic activity results, a fewer number of cells were detected in the soft SH-10 condition at day 3 compared to day 1 while the stiffer SH-30 showed the opposite trend. The denser network from SH-30 might provide the cells with a greater number of interaction points to adhere, enhancing proliferation as well. In addition, cells are known to perceive the physical signals induced by matrix stiffness and undergo modifications in morphology and proliferative potential due to the cascade of mechanotransduction events triggered by these physical cues.[75] Among the four GelMA-based hydrogels, it is noticeable the lower amount of

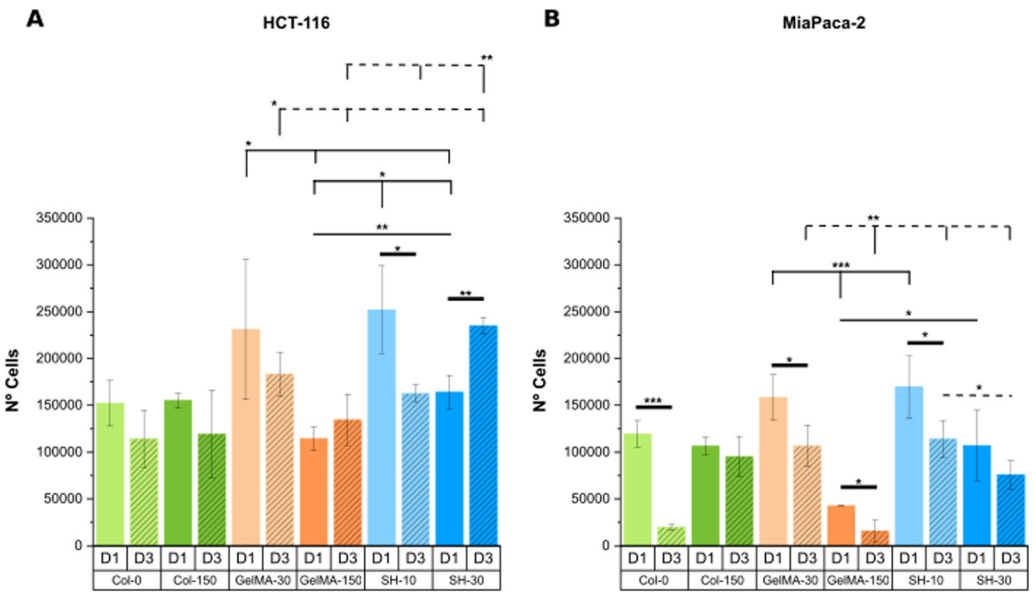


Fig. 10 DNA content is expressed as the number of HCT-116 (A) and MIA PaCa-2 cells (B) embedded within collagen and GelMA-based hydrogels on day-1 and day-3 (calibration curves are shown in Fig. S14, ESI†). Error bars SD. Note: ****$p < 0.0001$, ***$p < 0.001$, **$p < 0.01$, *$p < 0.05$. Thin and dashed lines represent statistics among scaffolds on day-1 and day-3, respectively. Thick lines correspond to statistical differences between day-1 and day-3 within the same condition. (Statistical differences towards Col-0 and Col-150 and non-statistical differences are not drawn in the graph – see Fig. S15, ESI†).

cells found in GelMA-150, presumably related with the higher mortality observed with live/dead staining. On the other hand, the number of MIA PaCa-2 cells encapsulated in the softer hydrogels GelMA-30 and SH-10 decreased over time (Fig. 10(B)) along with the also lower metabolic activity. We found an unexpectedly low amount of cells at day 3 in Col-0 and GelMA-150 hydrogels compared to the other conditions. Several studies have already reported that DNA content and metabolic activity do not necessarily correlate in all cases. Lim *et al.* observed that sharp rises in metabolic activity over time did not correspond to changes in the quantified cellular DNA of chondrocytes embedded in GelMA scaffolds[76] and Brand and coworkers pointed out that chemotaxis could be the reason for reporting a reduced DNA content in mucin-based hydrogels after 7 days of culture in spite of recording an increase in the metabolic activity of human mesenchymal stem cells.[77]

To conclude, a good alignment of results was generally found for the softest conditions (GelMA-30 and SH-10) in both cell lines HCT-116 and MIA PaCa-2, matching the decreased metabolic activity at day 3 with a lower quantified DNA content.

## Conclusions

The creation and evaluation of 3D scaffolds for cancer disease research has become a crucial step halfway from affordable simple 2D substrates and expensive complex *in vivo* models. Herein, we explore a platform of photopolymerized GelMA-based hydrogels with tunable stiffness as biomimetic 3D models for colorectal and pancreas diseases. We found that hydrogels prepared without methanol in the initial formulation exhibited lower mechanical properties than those with methanol but same trends and capability to tune stiffness although in a lower range of values. Besides, cell viability displayed an exceptional increase in hydrogels formulated without methanol.

Thus, in addition to the outstanding biological performance shown in semi-3D experiments from our earlier work, GelMA-based scaffolds also exhibited excellent cytocompatibility in 3D cell culture assays performed with two tumoral cell lines, HCT-116 and MIA PaCa-2 cells. HCT-116 cells cultured in collagen and GelMA-based hydrogels showed a clustering growth pattern with cell aggregates of different sizes over time which changed in response to the surrounding network. These results evidenced that less densely crosslinked and softer matrices represent permissive microenvironments for cell growth and migration. Linked to this cell motility, real-time monitoring revealed individual and collective migration of HCT-116 and MIA PaCa-2 cells. On the other hand, the formation of HCT-116 cellular clusters as a function of time pointed out the suitability of collagen and GelMA scaffolds to recreate the tumor cell microenvironment. HCT-116 cell line presented abundant filopodia formation which is in good agreement with its migratory behavior. Finally, the measured metabolic activity underwent a significant increase in stiffer hydrogels over the cell culture time while soft scaffolds promoted a drastic reduction. This proliferative and metabolically active phenotype developed within stiff networks matches with the malignant behavior observed in cancerous tissue.

In conclusion, we have demonstrated the ability of our GelMA-based material platform to create three dimensional microenvironments with different chemical composition, swelling behavior and stiffness and how HCT-116 and MIA PaCa-2 cells responded distinctly to the surrounding photocrosslinked matrix. This research establishes an attractive basis for further and more complex tumor models comprising concentration and stiffness gradients or co-culture with cancer associated fibroblasts (CAF), among others.

## Author contributions

The manuscript was written through contributions of all authors. All authors have given approval to the final version of the manuscript.

## Conflicts of interest

There are no conflicts of interest to declare.

## Acknowledgements

Authors acknowledge the use of instrumentation as well as the technical advice provided by the NMR Service of CEQMA (UZ-CSIC), Microscopy and Imaging Core Facility, (IACS-IISAragon) and ''Servicio General de Apoyo a la Investigación (SAI)'' This work was funded through projects PID2020-118485RB-I00 and PID2022-141276OB-I00 granted by MICIU/AEI/10.13039/501100011033 and by ''ERDF A way of making Europe''; through grant LMP221_21 funded by Gobierno de Aragón and ''ERDF A way of making Europe''; and, through the ''Fondo Social Europeo'' (DGA E15_23R). This research was also supported by CIBER -Consorcio Centro de Investigación Biomédica en Red-(CB06/01/00263), Instituto de Salud Carlos III, Ministerio de Ciencia e Innovación. RPC acknowledges Gobierno de Aragón for a predoctoral fellowship (2017-2021). SGL was funded by Spanish MINECO fellowship (DI-17-09585).

## References

1 L. Chin, Y. Xia, D. E. Discher and P. A. Janmey, *Curr. Opin. Chem. Eng.*, 2016, **11**, 77–84.
2 X. Tang, T. B. Kuhlenschmidt, J. Zhou, P. Bell, F. Wang, M. S. Kuhlenschmidt and T. A. Saif, *Biophys. J.*, 2010, **99**, 2460–2469.
3 A. J. Rice, E. Cortes, D. Lachowski, B. C. H. Cheung, S. A. Karim, J. P. Morton and A. Del Río Hernández, *Oncogenesis*, 2017, **6**, 1–9.
4 S. Lee and S. Kumar, *F1000Research*, 2016, **5**, 2261.
5 A. Singh, N. Dalal and P. Tayalia, *Biomed. Mater.*, 2023, **18**, 25010.
6 A. I. Van Den Bulcke, *Biomacromolecules*, 2000, **1**, 31–38.

 

7 Y. Zhang, H. Chen and J. Li, *Int. J. Biol. Macromol.*, 2022, **221**, 91–107.
8 A. D. Aryaa, P. M. Hallur, A. G. Karkisaval, A. Gudipati, S. Rajendiran, V. Dhavale, B. Ramachandran, A. Jayaprakash, N. Gundiah and A. Chaubey, *ACS Appl. Mater.*, 2016, **8**, 22005–22017.
9 N. Peela, F. S. Sam, W. Christenson, D. Truong, A. W. Watson, G. Mouneimne, R. Ros and M. Nikkhah, *Biomaterials*, 2016, **81**, 72–83.
10 R. Mazrouei, V. Velasco and R. Esfandyarpour, *Sci. Rep.*, 2020, **10**, 14669.
11 F. Fu, L. Shang, F. Zheng, Z. Chen, H. Wang, J. Wang, Z. Gu and Y. Zhao, *ACS Appl. Mater. Interfaces*, 2016, **8**, 13840–13848.
12 C.-Y. Chang, H. C. Johnson, O. Babb, M. L. Fishel and C.-C. Lin, *Acta Biomater.*, 2021, **130**, 161–171.
13 A. Rosenfeld, T. Göckler, M. Kuzina, M. Reischl, U. Schepers and P. A. Levkin, *Adv. Healthcare Mater.*, 2021, **10**, 2100632.
14 Y. Li, C. Liu, W. Liu, X. Cheng, A. Zhang, S. Zhang, C. Liu, N. Li and X. Jian, *Macromol. Biosci.*, 2021, **21**, 2100262.
15 G. C. J. Brown, K. S. Lim, B. L. Farrugia, G. J. Hooper and T. B. F. Woodfield, *Macromol. Biosci.*, 2017, **17**, 1–13.
16 N. Rajabi, M. Kharaziha, R. Emadi, A. Zarrabi, H. Mokhtari and S. Salehi, *J. Colloid Interface Sci.*, 2020, **564**, 155–169.
17 R. Pamplona, S. González-Lana, P. Romero, I. Ochoa, R. Martín-Rapún and C. Sánchez-Somolinos, *ACS Appl. Polym. Mater.*, 2023, **5**, 1487–1498.
18 C. E. Hoyle and C. N. Bowman, *Angew. Chem., Int. Ed.*, 2010, **49**, 1540–1573.
19 H. Y. Liu, M. Korc and C. C. Lin, *Biomaterials*, 2018, **160**, 24–36.
20 M. Devarasetty, E. Wang, S. Soker and A. Skardal, *Biofabrication*, 2017, **9**, 021002.
21 F. Cadamuro, L. Marongiu, M. Marino, N. Tamini, L. Nespoli, N. Zucchini, A. Terzi, D. Altamura, Z. Gao, C. Giannini, G. Bindi, A. Smith, F. Magni, S. Bertini, F. Granucci, F. Nicotra and L. Russo, *Carbohydr. Polym.*, 2023, **302**, 120395.
22 A. Williams, J. F. Nowak, R. Dass, J. Samuel and K. L. Mills, *Front. Physiol.*, 2018, **9**, 1–10.
23 E. Jabbari, S. K. Sarvestani, L. Daneshian and S. Moeinzadeh, *PLoS One*, 2015, **10**, e0132377.
24 N. Betriu, A. Andreeva, A. Alonso and C. E. Semino, *Biomedicines*, 2022, **10**, 1835.
25 T. J. Puls, X. Tan, C. F. Whittington and S. L. Voytik-Harbin, *PLoS One*, 2017, **12**, e0188870.
26 H. Shirahama, B. H. Lee, L. P. Tan and N. J. Cho, *Sci. Rep.*, 2016, **6**, 1–11.
27 A. F. S. A. Habeeb, *Anal. Biochem.*, 1966, **14**, 328–336.
28 E. Hoch, C. Schuh, T. Hirth, G. E. M. Tovar and K. Borchers, *J. Mater. Sci.: Mater. Med.*, 2012, **23**, 2607–2617.
29 B. H. Lee, H. Shirahama, N. J. Cho and L. P. Tan, *RSC Adv.*, 2015, **5**, 106094–106097.
30 C. Claaßen, M. H. Claaßen, V. Truffault, L. Sewald, G. E. M. Tovar, K. Borchers and A. Southan, *Biomacromolecules*, 2018, **19**, 42–52.
31 M. Monfared, M. D. Nothling, D. Mawad and M. H. Stenzel, *Biomacromolecules*, 2021, **22**, 4295–4305.
32 X. Li, S. Chen, J. Li, X. Wang, J. Zhang, N. Kawazoe and G. Chen, *Polymers*, 2016, **8**, 269.
33 L. Li, C. Lu, L. Wang, M. Chen, J. White, X. Hao, K. M. McLean, H. Chen and T. C. Hughes, *ACS Appl. Mater. Interfaces*, 2018, **10**, 13283–13292.
34 S. Bertlein, G. Brown, K. S. Lim, T. Jungst, T. Boeck, T. Blunk, J. Tessmar, G. J. Hooper, T. B. F. Woodfield and J. Groll, *Adv. Mater.*, 2017, **29**, 1–6.
35 R. Pamplona, S. González-Lana, P. Romero, I. Ochoa, R. Martín-Rapún and C. Sánchez-Somolinos, *Macromol. Biosci.*, 2023, **23**, 2300227.
36 R. Schrieber and H. Gareis, *Gelatine Handbook: Theory and Industrial Practice*, 2007.
37 J. Van Hoorick, P. Gruber, M. Markovic, M. Tromayer, J. Van Erps, H. Thienpont, R. Liska, A. Ovsianikov, P. Dubruel and S. Van Vlierberghe, *Biomacromolecules*, 2017, **18**, 3260–3272.
38 S. Xiao, T. Zhao, J. Wang, C. Wang, J. Du, L. Ying, J. Lin, C. Zhang, W. Hu, L. Wang and K. Xu, *Stem Cell Rev. Rep.*, 2019, **15**, 664–679.
39 J. Van Hoorick, L. Tytgat, A. Dobos, H. Ottevaere, J. Van Erps, H. Thienpont, A. Ovsianikov, P. Dubruel and S. Van Vlierberghe, *Acta Biomater.*, 2019, **97**, 46–73.
40 G. Miquelard-Garnier, S. Demeures, C. Creton and D. Hourdet, *Macromolecules*, 2006, **39**, 8128–8139.
41 S. T. Nguyen, H. T.-L. Nguyen and K. D. Truong, *Biomed. Res. Ther.*, 2020, **7**, 3855–3859.
42 E. E. Antoine, P. P. Vlachos and M. N. Rylander, *Tissue Eng., Part B*, 2014, **20**, 683–696.
43 A. Rubiano, D. Delitto, S. Han, M. Gerber, C. Galitz, J. Trevino, R. M. Thomas, S. J. Hughes and C. S. Simmons, *Acta Biomater.*, 2018, **67**, 331–340.
44 S. Ramanujan, A. Pluen, T. D. Mckee, E. B. Brown, Y. Boucher and R. K. Jain, *Biophys. J.*, 2002, **83**, 1650–1660.
45 B. N. Mason, J. P. Califano and C. A. Reinhart-King, *Matrix Stiffness: a regulator of cellular behavior and tissue formation*, 2012.
46 H. Yu, J. K. Mouw and V. M. Weaver, *Trends Cell Biol.*, 2011, **21**, 47–56.
47 S. Van Helvert and P. Friedl, *ACS Appl. Mater. Interfaces*, 2016, **8**, 21946–21955.
48 N. R. Richbourg, M. K. Rausch and N. A. Peppas, *Polymer*, 2022, **258**, 125316.
49 C. B. Raub, A. J. Putnam, B. J. Tromberg and S. C. George, *Acta Biomater.*, 2010, **6**, 4657–4665.
50 Y. Ishibashi, R. Haraguchi, S. Aoki, Y. Oishi and T. Narita, *Gels*, 2023, **9**, 458.
51 K. Maeda, *Cosmetics*, 2018, **5**, 14.
52 W. Tomal and J. Ortyl, *Polymers*, 2020, **12**, 1073.
53 M. Wang, J. Bai, K. Shao, W. Tang, X. Zhao, D. Lin, S. Huang, C. Chen, Z. Ding and J. Ye, *Int. J. Polym. Sci.*, 2021, **2021**, 1–16.
54 S. Kawano, M. Kojima, Y. Higuchi, M. Sugimoto, K. Ikeda, N. Sakuyama, S. Takahashi, R. Hayashi, A. Ochiai and N. Saito, *Cancer Sci.*, 2015, **106**, 1232–1239.
55 M. Nebuloni, L. Albarello, A. Andolfo, C. Magagnotti, L. Genovese, I. Locatelli, G. Tonon, E. Longhi, P. Zerbi,

R. Allevi, A. Podestà, L. Puricelli, P. Milani, A. Soldarini, A. Salonia and M. Alfano, *Sci. Rep.*, 2016, **6**, 22522.
56 T. Billiet, B. Van Gasse, E. Gevaert, M. Cornelissen, J. C. Martins and P. Dubruel, *Macromol. Biosci.*, 2013, **13**, 1531–1545.
57 A. Sionkowska, *Polym. Degrad. Stab.*, 2000, **68**, 147–151.
58 Z. Mũnoz, H. Shih and C. Lin, *Biomater. Sci.*, 2014, **2**, 1063.
59 B. D. Polizzotti, B. D. Fairbanks and K. S. Anseth, *Biomacromolecules*, 2008, **9**, 1084–1087.
60 D. J. Lavalley, P. G. Miller and M. L. Shuler, *Biotechnol. Prog.*, 2020, **37**, e3105.
61 L. Shah, A. Latif, K. J. Williams and A. Tirella, *Acta Biomater.*, 2022, **152**, 273–289.
62 M. Cavo, M. Fato, L. Peñuela, F. Beltrame, R. Raiteri and S. Scaglione, *Sci. Rep.*, 2016, **6**, 35367.
63 D. Loessner, K. S. Stok, M. P. Lutolf, D. W. Hutmacher, J. A. Clements and S. C. Rizzi, *Biomaterials*, 2010, **31**, 8494–8506.
64 M. Palmiero, I. Cantarosso, L. di Blasio, V. Monica, B. Peracino, L. Primo and A. Puliafito, *Mol. Oncol.*, 2023, **17**, 1699–1725.
65 K. Tanner, H. Mori, R. Mroue, A. Bruni-Cardoso and M. J. Bissell, *Proc. Natl. Acad. Sci. U. S. A.*, 2012, **109**, 1973–1978.
66 A. Yamamoto, A. E. Doak and K. J. Cheung, *Annu. Rev. Pathol.: Mech. Dis.*, 2023, **18**, 231–256.
67 M. M. Brás, T. B. Cruz, A. F. Maia, M. J. Oliveira, S. R. Sousa, P. L. Granja and M. Radmacher, *Cancers*, 2022, **14**, 5053.
68 Y. F. Zeng, Y. S. Xiao, Y. Liu, X. J. Luo, L. D. Wen, Q. Liu and M. Chen, *World J. Gastroenterol.*, 2018, **24**, 3884–3897.
69 P. K. Mattila and P. Lappalainen, *Nat. Rev. Mol. Cell Biol.*, 2008, **9**, 446–454.
70 A.-M. Baker, D. Bird, G. Lang, T. R. Cox and J. T. Erler, *Oncogene*, 2013, **32**, 1863–1868.
71 N. Davidenko, C. F. Schuster, D. V. Bax, R. W. Farndale, S. Hamaia, S. M. Best and R. E. Cameron, *J. Mater. Sci.: Mater. Med.*, 2016, **27**, 148.
72 K. M. Pawelec, S. M. Best and R. E. Cameron, *J. Mater. Chem. B*, 2016, **4**, 6484–6496.
73 R. Ata and C. Antonescu, *Int. J. Mol. Sci.*, 2017, **18**, 189.
74 C. Kremslehner, A. Miller, R. Nica, I. M. Nagelreiter, M. S. Narzt, B. Golabi, V. Vorstandlechner, M. Mildner, J. Lachner, E. Tschachler, F. Ferrara, K. Klavins, M. Schosserer, J. Grillari, A. Haschemi and F. Gruber, *Redox Biol.*, 2020, **37**, 101583.
75 B. Deng, Z. Zhao, W. Kong, C. Han, X. Shen and C. Zhou, *J. Transl. Med.*, 2022, **20**, 540.
76 K. S. Lim, B. J. Klotz, G. C. J. Lindberg, F. P. W. Melchels, G. J. Hooper, J. Malda, D. Gawlitta and T. B. F. Woodfield, *Macromol. Biosci.*, 2019, **19**, 1–14.
77 J. S. Brand, L. Forster, T. Böck, P. Stahlhut, J. Teßmar, J. Groll and K. Albrecht, *Macromol. Biosci.*, 2022, **22**, 2100274.

 